BOREAL ENVIRONMENT RESEARCH 12: 535–550 ISSN 1239-6095
Helsinki 24 October 2007 © 2007

FinROSE — middle atmospheric chemistry transport model

Juhani Damski[1)], Laura Thölix[1)], Leif Backman[1)]*, Petteri Taalas[2)] and Markku Kulmala[3)]

[1)] *Research and Development, Finnish Meteorological Institute, P.O. Box 503, FI-00101 Helsinki, Finland*
[2)] *Regional and Technical Cooperation for Development Department (RCD), World Meteorological Organization, Case Postale 2300, CH-1211 Genève 2, Suisse*
[3)] *Division of Atmospheric Sciences, P.O. Box 64, FI-00014 University of Helsinki, Finland*

Received 5 July 2006, accepted 14 Dec. 2006 (Editor in charge of this article: Veli-Matti Kerminen)

Damski, J., Thölix, L., Backman, L., Taalas, P. & Kulmala, M. 2007: FinROSE — middle atmospheric chemistry transport model. *Boreal Env. Res.* 12: 535–550.

In this paper we describe the development and performance of a three-dimensional global middle atmospheric chemistry transport model FinROSE. The FinROSE chemistry transport model includes a numerical scheme for stratospheric chemistry with parameterizations for heterogeneous processing on polar stratospheric clouds (PSC) and on liquid binary aerosols together with a parameterisation of large nitric acid trihydrate particles (i.e. NAT-rocks) and PSC sedimentation. The total number of trace species in the model is 34 and the total number of gas-phase reactions, photodissociation processes and heterogeneous reactions is about 150. The model is forced by external wind and temperature fields. The simulations are normally performed in a 5° × 10° (lat. × long.) grid from the surface up to around 0.1 hPa, with a vertical resolution of ca. 1.5 km in the stratosphere. Long-term simulations (40 to 50 years) have been done using winds and temperatures from ECMWF ERA40 analyses. The performance of the model in describing the stratospheric composition and chemistry is shown and evaluated in this paper. In general, the FinROSE results show a good comparison with measured total ozone. Also the timing, the depth and the deepening of the Antarctic ozone hole, and the responsible processes are captured well in the model simulations.

Introduction

The discovery of the Antarctic "ozone hole" in the mid-1980s was the start of an intensive international effort to understand the reasons behind polar ozone loss. Quite soon the impact of polar stratospheric clouds forming under low polar-winter stratospheric temperatures was recognized as the reason behind the high levels of active chlorine and low levels of atmospheric nitrogen (e.g. Crutzen and Arnold 1986, Solomon *et al*. 1986, Brasseur *et al*. 1990, Fahey *et al*. 1990). At present, the connections between the springtime ozone destruction, the amount of chlorine and other active halogen species and polar stratospheric clouds are well known (e.g. Solomon 1999, WMO 2003).

The assessment of the processes associated with the ozone depletion relies typically on both measurements and model studies. Due to the large number of parameters that one should measure simultaneously and also taking into

account the needed measurement frequency, it is difficult (or even impossible) to take a global 'snapshot' of the atmosphere where all significant parameters are simultaneously measured. The use of numerical models provides one way for these kinds of studies. A chemistry transport model (CTM) is typically an off-line model, which means that the meteorological input is taken from a model that solves atmospheric dynamics by itself. Off-line refers especially to the condition when the changes in atmospheric composition do not affect the modelled atmospheric dynamics or thermodynamics. The opposite would be a coupled-chemistry model where the effect of the atmospheric composition is taken into account by using a radiation transfer algorithm that solves the heating and cooling rates.

During the last decade, the production of many halocarbons has been regulated by the Montreal protocol (UNEP 2000). The common understanding at the moment is that the abundances of ozone-depleting substances in the atmosphere have peaked and are now declining (e.g. WMO 2003). Therefore the possible ozone layer recovery has been raised into discussions. Another hot topic has recently been the effect of enhanced greenhouse effect on the stratospheric ozone, due to the links between climate change and ozone depletion (WMO 2003). The increasing amounts of the so-called greenhouse gases such as carbon dioxide, methane, nitrous oxide and stratospheric water vapour is expected to cause cooling in the stratosphere (e.g. WMO 2003, Shine *et al*. 2003). This potential cooling may have dramatic effects on ozone layer, particularly over the high northern latitudes (Austin *et al*. 1992, Shindell *et al*. 1998). However, the effect of possible changes in the dynamics due to the enhanced greenhouse effect is presently not well known (WMO 2003). The observed global annual mean cooling of the stratosphere that has taken place over the past two decades is also coupled with the ozone depletion, as there is less ozone in the stratosphere to absorb solar radiation (e.g. WMO 2003); i.e. several open questions regarding the future evolution of stratospheric ozone still remain.

In order to ensure an up-to-date treatment of stratospheric processes and comparability to other similar existing CTMs, the chemical-transport model FinROSE (FinROSE-ctm) was developed and improved in several ways. These improvements include replacement of the advection scheme (Lin and Rood 1996), replacement of the photodissociation calculation scheme (Kylling 1992, Kylling *et al*. 1997, Mayer *et al*. 1998), updates to the chemical kinetics (e.g. Sander 2002), improvements to the heterogeneous processing, and updates to the description of the chemical mechanisms of the model. The description of the troposphere, as well as initial and boundary conditions has also been rewritten. Several other similar global CTMs have been developed during recent years (e.g. Lefèvre *et al*. 1998, Chipperfield 1999, 2003, 2006, Rummukainen *et al*. 1999, Egorova *et al*. 2001) and applied for multi-annual simulations.

The purpose of this paper is to introduce and describe the chemistry transport model FinROSE-ctm and to give a basic description of the model and show some examples of the model performance. The examples were chosen to show the stability of the model in long-term simulations, to show the climatological distribution of total ozone as well as the vertical distribution of ozone and finally to show the description of the basic processes related to polar ozone loss. The results are not analyzed in detail but some comparisons with satellite and sounding data were done. In this study the chosen example simulations were all based on the use of ERA40 data (Simmons and Gibson 2000) as meteorological forcing. The main goal of this paper is to show that the FinROSE model is applicable for model studies in different timescales (seasonal, decadal).

Model description

Gas-phase chemistry scheme

The original gas-phase chemistry scheme in FinROSE was based on the family-concept as formulated by Rose and Brasseur (1989). This concept is based on grouping, i.e. lumping, the fast reacting species, like odd oxygen, into chemical families. These families in turn have chemical lifetimes longer than the typical transport timescales. The basic idea of the family-approach is

to use quasi-steady state relations to solve the mixing ratios of the individual family members, since they typically establish photochemical equilibrium (PCE) with each other almost immediately in the sun-lit stratosphere. The FinROSE chemistry scheme has been designed mainly for stratospheric studies. Tropospheric chemistry is not included and the tropospheric abundances are given as boundary conditions. Ion-chemistry in the upper mesosphere has also been neglected; i.e. applicability of the model, in general, falls within the domain limited by the tropopause and the mesopause (i.e. around 10 km and 80 km, respectively). The model does not have explicit treatment of the source gases like CFCs, instead prescribed projections of the long-lived tracers like total inorganic chlorine (Cl_x) and bromine (Br_x) are used.

In total, eight chemical families have been defined in FinROSE, i.e. odd oxygen, odd hydrogen, carbon chemistry, reactive nitrogen, inorganic chlorine and inorganic bromine (Table 1). The mass conservation of the three large families, total inorganic chlorine (Cl_x), total inorganic bromine (Br_x) and total reactive nitrogen (NO_y) are ensured. Water vapour and methane are treated as individual species. The odd hydrogen family is short-lived and therefore not transported. The FinROSE model contains 28 transported tracers (Table 2), as well as 15 species in photochemical equilibrium (Table 3). Note that the list for the transported tracers also includes time tracers for type-Ia and type-II PSCs.

Table 1. Chemical families in FinROSE.

Family name	Symbol	Members
Odd oxygen	O_x	$O(^3P)$, O_3, $O(^1D)$
Odd hydrogen	HO_x	H, OH, HO_2
Oxides of nitrogen	NO_x	NO, NO_2
Reactive chlorine	ClO_x	Cl, ClO, Cl_2O_2
Reactive bromine	BrO_x	Br, BrO, BrCl
Total inorganic bromine	Br_x	BrO_x, HOBr, HBr, $BrONO_2$
Total inorganic chlorine	Cl_x	ClO_x, OClO, HCl, $ClONO_2$, HOCl, Cl_2, $ClNO_2$, BrCl
Total nitrogen	NO_y	NO_x, HNO_3, N_2O_5, HO_2NO_2, $ClONO_2$, $ClNO_2$, $BrONO_2$, NO_3, N

Table 2. Long-lived, i.e. transported species in FinROSE.

Constituent	Symbol	Family
Nitrous oxide	N_2O	–
Methane	CH_4	–
Water vapour	H_2O	–
Odd nitrogen	NO_y	–
Nitric acid	HNO_3	NO_y
Dinitrogen pentoxide	N_2O_5	NO_y
Total model chlorine	Cl_x	–
Total model bromine	Br_x	–
Odd oxygen	O_x	O_x
Carbon monoxide	CO	–
Chlorine dioxide	OClO	Cl_x
PSC(type-Ia)-tracer	PSC(I), NAT	–
PSC(type-II)-tracer	PSC(II), ice	–
Chlorine nitrate	$ClONO_2$	Cl_x, NO_y
Hypochlorous acid	HOCl	Cl_x
Chlorine molecule	Cl_2	Cl_x
Hydrogen peroxide	H_2O_2	–
Chlorine nitrite	$ClNO_2$	Cl_x, NO_y
Hydrogen bromide	HBr	Br_x
Bromine nitrate	$BrONO_2$	Br_x
Oxides of nitrogen	NO_x	NO_y
Peroxy nitric acid	HO_2NO_2	NO_y
Active chlorine	ClO_x	Cl_x
Active bromine	BrO_x	Br_x
Dichlorine peroxide (ClO-dimer)	Cl_2O_2	Cl_x
Hypobromous acid	HOBr	Br_x
Hydrochloric acid	HCl	Cl_x
Formaldehyde	CH_2O	–

Table 3. Short-lived species in FinROSE.

Constituent	Symbol	Family
Exited state oxygen	$O(^1D)$	O_x
Hydroxyl radical	OH	HO_x
Atomic chlorine	Cl	Cl_x
Ground state atomic oxygen	O i.e. $O(^3P)$	O_x
Ozone	O_3	O_x
Hydroperoxy radical	HO_2	HO_x
Nitrogen dioxide	NO_2	NO_x, NO_y
Nitric oxide	NO	NO_x, NO_y
Atomic bromine	Br	BrO_x, Br_x
Atomic nitrogen	N	NO_y
Chlorine monoxide	ClO	ClO_x, Cl_x
Bromine monoxide	BrO	BrO_x, Br_x
Nitrogen trioxide	NO_3	NO_y
Bromine monochloride	BrCl	Br_x, BrO_x, Cl_x
Atomic hydrogen	H	HO_x

There are 114 homogeneous reactions included in FinROSE (Table 4). In addition, 30 photodissociation processes are used (Table 5). The chemical kinetic data, reaction rate constants and absorption cross-sections are based on the tabulations given by DeMore *et al*. (1997) and Sander *et al*. (2002). The photodissociation frequencies in FinROSE are calculated using PHODIS-radiative transfer model (Kylling *et al*. 1997, Mayer *et al*. 1998). The PHODIS model version used in this study includes multiple scattering (up to eight orders), absorption by O_2 and O_3 and the effect of surface albedo. The wavelength range of the model is from about 116 to 735 nm (i.e. in the UV visible range). Since the explicit run-time solving of photodissociation coefficients in the FinROSE 3-D grid with a typical time-step would be too expensive, the photodissociation frequencies have been pre-calculated into lookup-tables. The tabulation of these tables is based on the altitude, solar zenith angle, ozone amounts and surface albedo. The surface albedo,

Table 4. The homogeneous reactions in the FinROSE chemistry scheme, organized by the main families.

O_x chemistry

$O + O + M$	$\rightarrow O_2 + M$
$O + O_2 + M$	$\rightarrow O_3 + M$
$O + O_3$	$\rightarrow O_2 + O_2$
$O(^1D) + N_2$	$\rightarrow O + N_2$
$O(^1D) + O_2$	$\rightarrow O + O_2$
$O(^1D) + O_3$	$\rightarrow O_2 + O_2$
$O(^1D) + O_3$	$\rightarrow O_2 + O + O$
$O(^1D) + N_2$	$\rightarrow N_2O$

HO_x chemistry

$H + O_2 + M$	$\rightarrow HO_2 + M$
$O(^1D) + H_2O$	$\rightarrow OH + OH$
$H + O_3$	$\rightarrow OH + O_2$
$O(^1D) + H_2$	$\rightarrow OH + H$
$O + OH$	$\rightarrow O_2 + H$
$OH + O_3$	$\rightarrow HO_2 + O_2$
$HO_2 + O_3$	$\rightarrow OH + O_2 + O_2$
$O + HO_2$	$\rightarrow OH + O_2$
$OH + HO_2$	$\rightarrow H_2O + O_2$
$OH + H_2$	$\rightarrow H_2O + H$
$H + HO_2$	$\rightarrow OH + OH$
$H + HO_2$	$\rightarrow H_2 + O_2$
$H + HO_2$	$\rightarrow H_2O + O$
$HO_2 + HO_2$	$\rightarrow H_2O_2 + O_2$
$OH + H_2O_2$	$\rightarrow H_2O + HO_2$
$OH + CO$	$\rightarrow CO_2 + H$
$H_2O_2 + O$	$\rightarrow OH + HO_2$
$OH + OH$	$\rightarrow O + H_2O$
$OH + OH + M$	$\rightarrow H_2O_2 + M$

Carbon chemistry

$CH_4 + O(^1D)$	$\rightarrow CH_3 + OH$
$CH_4 + OH$	$\rightarrow CH_3 + H_2O$
$CH_2O + OH$	$\rightarrow CHO + H_2O$
$CH_2O + O$	$\rightarrow CHO + OH$

NO_y chemistry

$O + NO_2$	$\rightarrow NO + O_2$
$O_3 + NO$	$\rightarrow NO_2 + O_2$
$N + NO$	$\rightarrow N_2 + O$
$N + O_2$	$\rightarrow NO + O$
$O_3 + NO_2$	$\rightarrow NO_3 + O_2$
$NO_2 + NO_3 + M$	$\rightarrow N_2O_5 + M$
$N_2O_5 + M$	$\rightarrow NO_2 + NO_3 + M$
$OH + NO_2 + M$	$\rightarrow HNO_3 + M$
$HO_2 + NO_2 + M$	$\rightarrow HO_2NO_2 + M$
$HO_2NO_2 + M$	$\rightarrow HO_2 + NO_2 + M$
$HNO_3 + OH$	$\rightarrow H_2O + NO_3$
$OH + HO_2NO_2$	$\rightarrow H_2O + NO_2 + O_2$
$O(^1D) + N_2O$	$\rightarrow N_2 + O_2$
$O(^1D) + N_2O$	$\rightarrow NO + NO$
$O + NO_3$	$\rightarrow O_2 + NO_2$
$OH + NO_3$	$\rightarrow HO_2 + NO_2$
$HO_2 + NO_3$	$\rightarrow OH + NO_2 + O_2$
$HO_2 + NO_3$	$\rightarrow HNO_3 + O$
$O + NO_2 + M$	$\rightarrow NO_3 + M$
$NO + O + M$	$\rightarrow NO_2 + M$
$NO + NO_3$	$\rightarrow NO_2 + NO_2$
$NO + HO_2$	$\rightarrow NO_2 + OH$
$H + NO_2$	$\rightarrow OH + NO$
$N + NO_2$	$\rightarrow N_2O + O$
$NO_2 + NO_3$	$\rightarrow NO + NO_2 + NO_2$
$NO_3 + NO_3$	$\rightarrow NO_2 + NO_2 + O_2$

Cl_x chemistry

$Cl + O_3$	$\rightarrow ClO + O_2$
$ClO + O$	$\rightarrow Cl + O_2$
$ClO + NO$	$\rightarrow NO_2 + Cl$
$Cl + CH_4$	$\rightarrow HCl + CH_3$
$Cl + H_2$	$\rightarrow HCl + H$
$Cl + HO_2$	$\rightarrow HCl + O_2$
$ClO + OH$	$\rightarrow Cl + HO_2$
$CH_2O + Cl$	$\rightarrow HCl + HCO$
$OH + HCl$	$\rightarrow H_2O + Cl$
$ClO + NO_2 + M$	$\rightarrow ClONO_2 + M$
$O + ClONO_2$	$\rightarrow ClO + NO_3$
$ClO + HO_2$	$\rightarrow HOCl + O_2$
$OH + HOCl$	$\rightarrow H_2O + ClO$
$O + HOCl$	$\rightarrow OH + ClO$
$Cl + NO_2 + M$	$\rightarrow ClNO_2 + M$
$Cl + HOCl$	$\rightarrow OH + Cl_2$
$ClO + OH$	$\rightarrow HCl + O_2$
$ClO + ClO$	$\rightarrow Cl + OClO$
$ClO + ClO$	$\rightarrow Cl_2 + O_2$
$ClO + ClO$	$\rightarrow Cl + Cl + O_2$
$ClO + ClO + M$	$\rightarrow Cl_2O_2 + M$
$Cl_2O_2 + M$	$\rightarrow ClO + ClO + M$
$OClO + OH$	$\rightarrow HOCl + O_2$
$Cl + OClO$	$\rightarrow ClO + ClO$
$OClO + O$	$\rightarrow ClO + O_2$
$OClO + O_3$	$\rightarrow ClO + O_2 + O_2$
$OClO + NO$	$\rightarrow NO_2 + ClO$
$Cl_2 + O(^1D)$	$\rightarrow Cl + ClO$
$Cl_2O_2 + Cl$	$\rightarrow Cl_2 + Cl + O_2$
$NO_3 + Cl$	$\rightarrow ClO + NO_2$
$ClO + NO_3$	$\rightarrow NO_2 + Cl + O_2$
$HCl + O(^1D)$	$\rightarrow Cl + OH$
$Cl_2 + OH$	$\rightarrow HOCl + Cl$
$Cl + ClONO_2$	$\rightarrow NO_3 + Cl_2$
$HO_2 + Cl$	$\rightarrow ClO + OH$
$H_2O_2 + Cl$	$\rightarrow HCl + HO_2$
$HCl + O$	$\rightarrow Cl + OH$
$ClONO_2 + OH$	$\rightarrow HOCl + NO_3$
$ClNO_2 + OH$	$\rightarrow HOCl + NO_2$

Br_x chemistry

$Br + O_3$	$\rightarrow BrO + O_2$
$BrO + O$	$\rightarrow Br + O_2$
$BrO + NO$	$\rightarrow NO_2 + Br$
$BrO + ClO$	$\rightarrow OClO + Br$
$BrO + ClO$	$\rightarrow Br + Cl + O_2$
$BrO + ClO$	$\rightarrow BrCl + O_2$
$BrO + BrO$	$\rightarrow Br + Br + O_2$
$Br + HO_2$	$\rightarrow HBr + O_2$
$Br + OClO$	$\rightarrow BrO + ClO$
$Br + CH_2O$	$\rightarrow HBr + HCO$
$OH + HBr$	$\rightarrow H_2O + Br$
$BrO + NO_2 + M$	$\rightarrow BrONO_2 + M$
$BrO + HO_2$	$\rightarrow HOBr + O_2$
$HBr + O(^1D)$	$\rightarrow OH + Br$
$OH + BrO$	$\rightarrow HO_2 + Br$
$OH + BrO$	$\rightarrow HBr + O_2$
$HBr + O$	$\rightarrow Br + OH$
$HOBr + O$	$\rightarrow BrO + OH$

however, has been kept constant (i.e. 30%). The implemented solar zenith angle range is extended down to 92.9°. Photolysis rates, which depend on e.g. local insolation and ozone column, are interpolated for each grid-point and time-step.

Heterogeneous chemistry scheme

The polar stratospheric clouds (PSCs) play a very important role in the process of polar ozone depletion due to the heterogeneous chlorine activation taking place on or in the PSC particles. Furthermore, gravitational sedimentation of PSC particles can cause significant denitrification and dehydration. The formation of PSCs is highly dependent on the temperature and the typical formation temperatures for the PSCs act as threshold barriers for chlorine activation and sedimentation processes. This means not only that the PSC schemes have to be well established, but also that the applied temperatures need to be accurate.

The heterogeneous chemistry scheme in FinROSE is based on the calculation of (i) the composition and volume of sulphate aerosols and PSCs and the partition of species between gas phase and condensed phase, (ii) the surface area densities, (iii) the heterogeneous reaction rate coefficients in or on sulphate aerosols and polar stratospheric cloud (PSC) particles, and (iv) the sedimentation of the PSC particles. Both hydrolysis processes and reactions with mineral acids (i.e. HCl and HBr) are included (Table 6). The heterogeneous chemistry in FinROSE takes into account liquid binary aerosols (LBA), i.e. sulphate aerosols consisting of sulphuric acid and water, type-Ia particles consisting of nitric acid trihydrate (NAT), type-Ib droplets consisting of sulphuric acid, nitric acid and water, i.e. super-cooled ternary solution (STS), as well as type-II PSC particles composed of water ice. In the PSC scheme a number density profile is given for each PSC type and the sulphuric acid distribution is calculated from SAGE data (Jackman *et al*. 1996, Rosenfield *et al*. 1997) or taken from 2-D model data (Bekki and Pyle 1992).

The treatment of LBA and STS droplets is based on a non-iterative method explained by Carslaw *et al*. (1995). The PSC scheme calculates both the composition and volume of these liquid aerosols and assumes that there is no activation barrier for the formation of STS from aerosols. The LBAs are assumed within a temperature range from 240 to 215 K and STSs below 215 K, but not below the water ice formation point. The number density profile of the sulphate aerosols is estimated from McLinden *et al*. (1999), which gives values from 0.1 to 15 cm^{-3}. The solubility of a gas phase component in an aerosol is calculated from its effective Henry's law constant.

The thermodynamic equilibrium equations given by Hanson and Mauersberger 1988 were used for the formation temperatures and vapour pressures above NAT particles. However, a supersaturation requirement (typically around 20) is used for the NAT formation. The evaporation of NAT particles is assumed to take place

Table 5. Photodissociation processes in the FinROSE chemistry scheme.

$O_2 + h\nu$	$\rightarrow O + O$	$OClO + h\nu$	$\rightarrow O + OClO$
$O_3 + h\nu$	$\rightarrow O + O_2$	$Cl_2O_2 + h\nu$	$\rightarrow Cl + ClO_2$
$H_2O + h\nu$	$\rightarrow H + OH$	$HCl + h\nu$	$\rightarrow H + C$
$N_2O + h\nu$	$\rightarrow N_2 + O(^1D)$	$Cl_2 + h\nu$	$\rightarrow Cl + Cl$
$CH_4 + h\nu$	$\rightarrow H + CH_3$	$CO_2 + h\nu$	$\rightarrow O + CO$
$NO_2 + h\nu$	$\rightarrow NO + O$	$ClNO_2 + h\nu$	$\rightarrow Cl + NO_2$
$HNO_3 + h\nu$	$\rightarrow OH + NO_2$	$BrONO_2 + h\nu$	$\rightarrow BrO + NO_2$
$HOCl + h\nu$	$\rightarrow OH + Cl$	$BrCl + h\nu$	$\rightarrow Br + Cl$
$HO_2NO_2 + h\nu$	$\rightarrow OH + NO_3$	$HOBr + h\nu$	$\rightarrow Br + OH$
$HO_2NO_2 + h\nu$	$\rightarrow HO_2 + NO_2$	$BrO + h\nu$	$\rightarrow Br + O$
$ClONO_2 + h\nu$	$\rightarrow Cl + NO_3$	$CH_2O + h\nu$	$\rightarrow H + CHO$
$ClONO_2 + h\nu$	$\rightarrow ClO + NO_2$	$CH_2O + h\nu$	$\rightarrow H_2 + CO$
$N_2O_5 + h\nu$	$\rightarrow NO_2 + NO_3$	$NO + h\nu$	$\rightarrow N + O$
$O_3 + h\nu$	$\rightarrow O(^1D) + O_2$	$NO_3 + h\nu$	$\rightarrow NO_2 + O$
$H_2O_2 + h\nu$	$\rightarrow OH + OH$	$NO_3 + h\nu$	$\rightarrow O + O_2$

Table 6. Heterogeneous reactions in the FinROSE PSC scheme.

$ClONO_2(g) + H_2O(s)$	$\rightarrow HOCl(g) + HNO_3(s)$
$BrONO_2(g) + H_2O(s)$	$\rightarrow HOBr(g) + HNO_3(s)$
$N_2O_5(g) + H_2O(s)$	$\rightarrow HNO_3(s) + HNO_3(s)$
$ClONO_2(g) + HCl(s)$	$\rightarrow Cl_2(g) + HNO_3(s)$
$HOCl(g) + HCl(s)$	$\rightarrow Cl_2(g) + H_2O(s)$
$BrONO_2(g) + HCl(s)$	$\rightarrow BrCl(g) + HNO_3(s)$
$HOBr(g) + HCl(s)$	$\rightarrow BrCl(g) + H_2O(s)$
$N_2O_5(g) + HCl(s)$	$\rightarrow ClNO_2(g) + HNO_3(s)$
$ClONO_2(g) + HBr(s)$	$\rightarrow BrCl(g) + HNO_3(s)$
$HOCl(g) + HBr(s)$	$\rightarrow BrCl(g) + H_2O(s)$

(s) = compound in condensed phase; (g) = compound in gas phase.

at the thermodynamic equilibrium (i.e. typically around 195 K). The number density of the NAT particles is initially assumed to be 1 cm^{-3} (e.g. Krämer *et al*. 2003). A scheme for the incorporation of large NAT particles (i.e. NAT-rocks) is based on the use of a transported NAT tracer. The growing of the aged NAT particles is taken into account using a simple parameterization based on the work by Fahey *et al*. (2001). The time requirement for the formation of NAT-rocks is set to 84 hours. In other words, NAT-rocks are produced by the model if, according to the NAT tracer, NAT particles have existed in an air mass continuously for three and a half days. After that the number density of NAT particles is reduced to 0.002 cm^{-3}, which increases the particle radius and volume accordingly. Coexistence of NAT and STS is allowed.

The water ice temperature threshold for the ice formation is calculated using the expressions of Marti and Mauersberger (1993) and Hanson and Mauersberger (1988) for the equilibrium pressures of HNO_3 over ice. The formation of ice is controlled by the supersaturation of H_2O, for which a threshold value of 1.4 is used, but the evaporation is assumed to take place at thermodynamic equilibrium. The ice number density is assumed to be 0.04 cm^{-3}, roughly in line with observations of synoptic scale PSCs (e.g. Dye *et al*. 1992). If water ice is formed, no other PSC particles are allowed.

In order account for the effect of hysteresis due to the supersaturation requirements the existence of NAT and ice is also transported as time tracers. This means that at any grid location where NAT or ice has formed (or previously existed), the ice tracer or NAT tracer is assigned or added a value of one time-step. The age of the NAT tracer is also used for the formation of large and faster sedimenting NAT particles. The formation of NAT and ice is controlled by the supersaturation with respect to HNO_3 and H_2O. The supersaturation requirements describe the NAT or ice nucleation barrier and also increase the significance of STS *vs*. NAT particles for chlorine activation.

The reaction rate coefficients for the heterogeneous processes are calculated according to the recommendations given by Sander *et al*. (2002) and Atkinson *et al*. (2000). The maximum kinetic mass flux is calculated from the kinetic gas theory, which is then scaled by the respective uptake coefficients to get the reaction rates. The uptake coefficients in turn take into account all processes controlling the mass transport (e.g. gas and liquid phase diffusion, mass accommodation and chemical reactions).

The sedimentation of the condensed species on ice, NAT or STS droplets is solved for H_2O, HNO_3 and NO_y, and the budgets of these species are adjusted accordingly to ensure mass conservation. Instantaneous mixing is assumed, and the sedimented fractions are added directly to the mixing ratios of H_2O, HNO_3 and NO_y at the corresponding level. The dissolved and/or adsorbed species (e.g. HCl or HBr) are not accounted for, i.e. not sedimented, due to the high reaction rates. The terminal velocities are based on the use of calculated average particle radii for each PSC type. The amounts of the sedimented constituents are known from the composition and number density of the particles. The sedimented fraction during one time-step can then be calculated using the terminal velocity of respective PSC particle type and thickness of the atmospheric layer.

Transport scheme

In FinROSE the transport is done separately from the chemistry, and each transported tracer is solved individually (Table 2). The transport in FinROSE is taken care of by calculating the horizontal mass fluxes using external horizontal winds and surface pressures and by solving the vertical fluxes internally. The transport of long-lived tracers in the FinROSE model is based on the semi-Lagrangian transport scheme (SLT). The idea of a SLT algorithm is to estimate the departure point of the air parcel that arrives at a particular grid location using the 3-D wind of this arriving location (*see* Smith 1995), and assign the value at the departure point to that grid point.

In FinROSE a flux-form semi-Lagrangian scheme (FSLT) developed by Lin and Rood (1996) is used. This scheme solves the three dimensional transport of volume mixing ratio fields. The horizontal transport is solved using

an un-constrained piece-wise parabolic method (PPM) together with a Zalesak-type multidimensional flux correction algorithm (Zalesak 1979). This flux correction basically ensures the positivity of the sub-grid tracer distributions. The PPM method itself is known to be nearly diffusion free. The vertical transport is based on the use of the Huynh/Van Leer/Lin full monotonicity constraint (for details *see* Lin *et al*. 1994, Lin and Rood 1996). The vertical velocities are solved internally as a residual by integrating the continuity equation from the top boundary to the lower boundary. The model boundaries are set at half vertical grid-length away from the highest and lowest model levels.

Numerical aspects

The model code (FORTRAN 77) has been made flexible to allow easy changes of the grid resolution. Therefore, the FinROSE model is capable of using driver input (e.g. winds and temperatures) from various sources. These sources include meteorological data from the European Centre for Medium-Range Weather Forecasts (ECMWF) or from a general circulation model (Damski 2005). Typically in multi-annual studies a horizontal resolution of five by ten degrees (latitude-longitude) is used. For case studies, when e.g. the distributions in the vicinity of the vortex edge are studied, a higher resolution can be used. The number of vertical levels is typically around 30 from the surface up to middle or upper mesosphere (i.e. around 60 to 85 km). Hybrid sigma-pressure levels similar to the ECMWF model levels are used, i.e. with sigma levels near the ground transitioning to pure pressure surfaces above ca. 60 hPa. In the meridional direction the model domain starts from latitude 90°S, and extends to 90°N.

The transport and chemistry of constituents having a lifetime longer than or similar to the typical atmospheric transport time scales is obtained by solving the continuity equation. During each time-step the tracer transport is first solved by the FSLT scheme and using these intermediate mixing ratios the tendency equation for the constituent due to the chemistry is obtained. A simple backward-Euler method is used for the integration of gas-phase concentrations of species in time. The production and loss rates are solved in the chemistry scheme for each long-lived tracer using the temperatures from the driver model and the mixing ratios for short-lived species, which are solved at every time-step using the photochemical equilibrium (PCE) assumption between the family members. The procedure is iterative. The timestep for the transport and chemistry is typically from 7.5 to 30 min.

Any potential inconsistencies between the chemical family mixing ratios and the sum of the family members are taken into account with a simple scaling scheme. After transport and chemistry at every time-step the mixing ratios of the family members are scaled to match the mixing ratio of the whole family.

Results and discussion

Model stability in long-term simulations

A basic requirement for any atmospheric model is a stable evolution of model integrations. For example in the case of multi-annual simulations, the evolution of atmospheric composition should take place without any loss or gain of atmospheric mass and the reproduced annual and seasonal variations should exhibit realistic variations. In order to demonstrate these stability requirements in the case of the FinROSE model performance, we show the temporal evolution of the total ozone column for one whole decade (Fig. 1). The model data are also compared with total ozone from TOMS satellite measurements and with the ERA40 ozone data (Dethof and Hólm 2004). The total ozone data are shown as global and hemispheric averages (Fig. 1, northern hemisphere in the top panel, southern hemisphere in the middle panel, and the whole globe in the bottom panel). The FinROSE results in this example are based on a multi-decadal simulation driven with ERA40 analyses of winds and temperatures used continuously from 1957 to 2002, i.e. the shown decade is already the third full ten-year period in the FinROSE simulation.

As seen from the TOMS data, a typical global average column of ozone during the

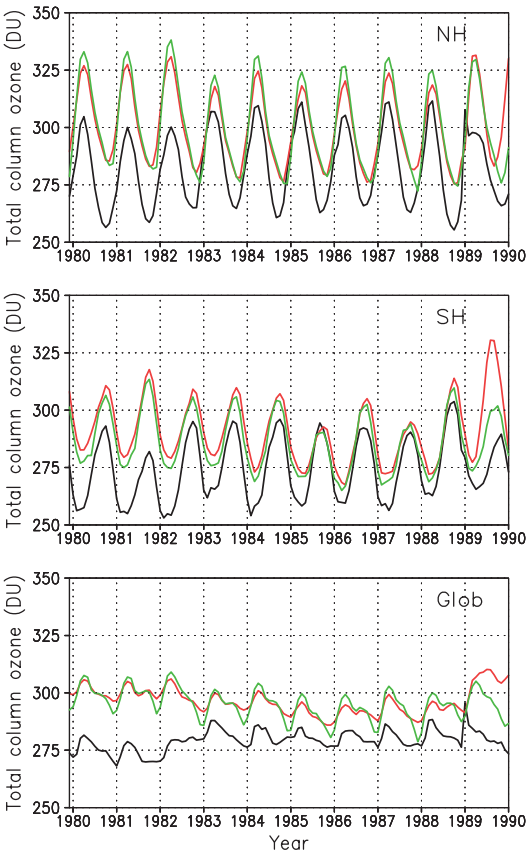

Fig. 1. Area averaged total column ozone: FinROSE (black), ERA40 (red) and TOMS-v8 (green). Top panel: northern hemisphere; middle panel: southern hemisphere; bottom panel: global total column ozone.

shown period varies from around 280 to 310 DU depending on the season and the year (Fig. 1). The measured annual total ozone amplitude is somewhat smaller than 20 DU. In most of the cases the evolution of the ERA40 ozone closely follows the measured TOMS total ozone (Fig. 1). This similarity is based on the fact that TOMS total ozone data have been widely used in the production of the ERA40 data through assimilation (Dethof and Hólm 2004). Since the discrepancies between the TOMS data and ERA40 data are outside the scope of this study, these differences are not discussed in detail. In general, the evolution of the FinROSE total ozone is stable during the whole model integration period (Fig. 1). The seasonal variations follow the observed patterns and the annual amplitude is just slightly less than the observed annual amplitude. Also the year-to-year variations in the annual amplitudes follow the measured changes. However, the absolute level of simulated total ozone differs from the measured global levels. The reproduced global average in the FinROSE-simulation is about 15 DU lower than respective TOMS measurements, except for the early 1980s where the simulated global ozone averages are clearly low as compared with measurements. Around 1982 there is a change in the meteorological data that increases the model global total ozone with about 10 DU. Since the overall evolution of the FinROSE simulated model ozone is acceptable this bias in absolute level should be considered as a model feature that derives both from the model design and from the used driver fields (ERA40 in this case). Furthermore, the differences between TOMS and ERA40 total ozone during 1989 to 1990 are due to the fact that the TOMS total ozone data were not assimilated into the ERA40 during that period (Fig. 1). As a result the ERA40 ozone is higher than the TOMS measurement, while the FinROSE result follows a similar pattern as during earlier simulated years.

From the hemispheric viewpoint the analysis is similar to the discussion given above for the whole globe (Fig. 1). The model evolutions are stable both over the southern hemisphere and over the northern hemisphere. However, over the northern hemisphere the simulated negative total ozone bias is somewhat more significant than over the southern hemisphere: The absolute level of the modelled total ozone in FinROSE is about 20 DU too low over the northern hemisphere and about 10 DU too low over the southern hemisphere. The seasonal and interannual variations are, however, nicely reproduced. For example over the southern hemisphere an ocular comparison shows an increasing trend in the minimum values onwards from year 1987 (middle panel in Fig. 1). This year-to-year change is very nicely simulated by the model. The model also captures nicely the overall hemispheric differences showing lower values for the southern hemisphere as compared with those for the northern hemisphere. However, the differences between the northern and southern hemispheres are slightly more significant in observations than in the model results (Fig. 1). A major cause for the dis-

crepancies between the measured and simulated column ozone lies in the reproduced Brewer-Dobson circulation, which in this example case seem to be too efficient (*see* e.g. van Noije *et al.* 2004). As mentioned before these types of features are derivatives of used meteorological driver fields as well as general model design.

Climatological distribution of ozone

An atmospheric model should be able to reproduce the seasonal and geographical patterns typically seen in ozone climatologies. For such comparison we use the ozone climatology compiled by Fortuin and Kelder (1998). This climatology is based on ozone sonde measurements and satellite measurements of ozone, covering the period from 1980 to 1991. The climatology was made consistent with the TOMS data. Zonally averaged monthly mean total column ozone data from FinROSE, of the corresponding period, were compared with the Fortuin and Kelder ozone climatology and TOMS-v8 satellite data (Fig. 2).

The general climatological patterns in the FinROSE results compare well with the ozone climatology and TOMS data (Fig. 2). The annual pattern is nicely reproduced with late winter early spring maxima, late summer early autumn minima, and Antarctic springtime depletion. However, there are some discrepancies between the simulations and observations. The modelled ozone fields are generally lower than observed, around 20 DU or less. The maximum values in the tropical vertical ozone profile above 30 hPa are too low, which results in a deficiency in total ozone, i.e. the photochemical equilibrium of the model is too low with respect to ozone. This can be a result of both an offset in the photochemical rates, i.e. ozone net production, and the too strong representation in the ERA40 data of the vertical transport in the tropics. These combined also seem to affect the overall equilibrium state of the model. However, the low tropical ozone also balances the strong Brewer-Dobson circulation to some extent and prevents the ozone amounts from overshooting at high latitudes. Also the northern hemispheric high latitude maximum is correctly timed, but somewhat less profound than in the measurements. The northern hemispheric mid-latitude ozone levels are quite well described, as will be shown in the next section (Fig. 3). Over the southern hemisphere the model overall performance is quite good. Especially the representation of the "ozone hole" is very well simulated. The time period, from 1980 to 1991, already includes the advent of the Antarctic ozone depletion, which is clearly seen both in the FinROSE model clima-

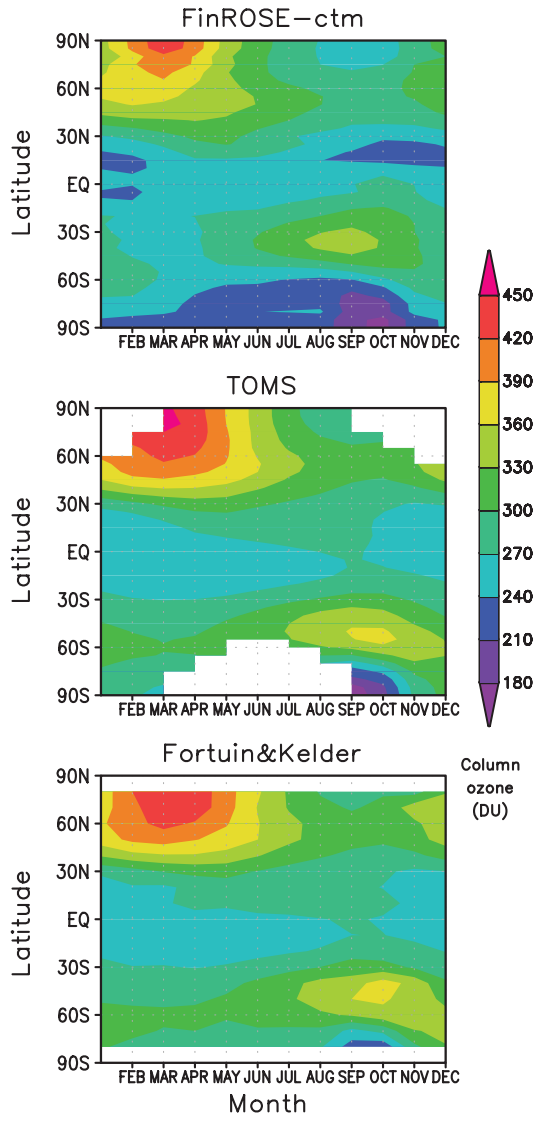

Fig. 2. Zonally averaged monthly mean total ozone climatologies for the 1980s. Top panel: FinROSE-ctm; Middle panel: TOMS-v8; Bottom panel: Fortuin and Kelder ozone climatology.

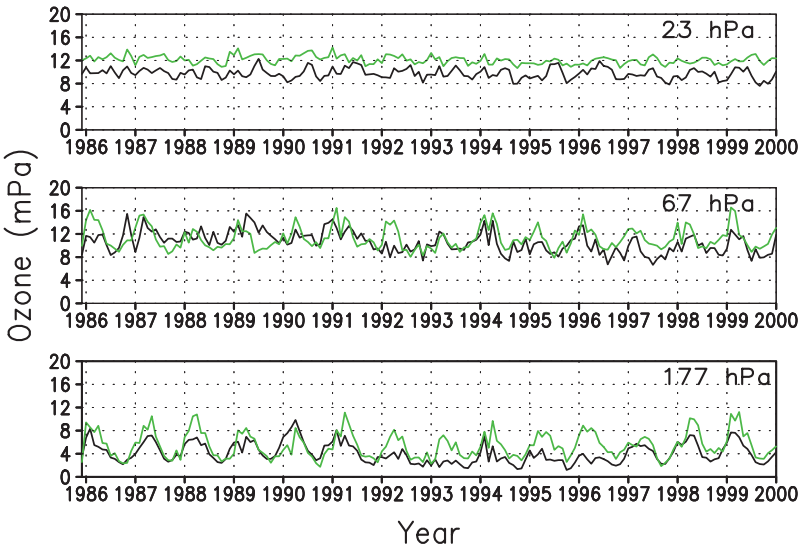

Fig. 3. Ozone partial pressure (mPa) above Payerne (46.5°N, 6.6°E) at 177, 67 and 23 hPa, FinROSE data in black and ozone soundings data in green.

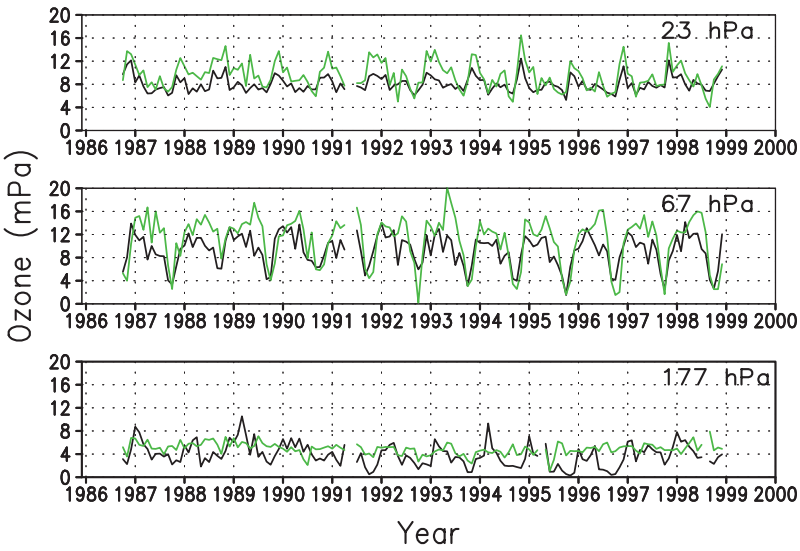

Fig. 4. Ozone partial pressure (mPa) above Syowa (69.0°S, 39.6°E) at 177, 67 and 23 hPa, FinROSE data in black and ozone sounding data in green.

tology and in the TOMS data (Fig. 2). However, the minimum values appear somewhat later in the model data than in the TOMS data. In addition, the location of the southern hemispheric mid-latitude springtime maximum is located too far north in the model and the maximum also occurs too early.

Ozone vertical distribution

As seen in the previous sections, the model is able to reproduce the observed latitude distribution as well as the seasonal behaviour of total ozone with some deficiencies. The evolution of ozone at different atmospheric levels in the model was compared with ozone sounding data from Payerne in Europe (46.5°N, 6.6°E, Fig. 3) and Syowa in Antarctica (69.0°S, 39.6°E, Fig. 4). The ozone profile data are averaged from data points above and below the model levels and the model results were interpolated to the station coordinates. The monthly mean ozone partial pressure (mPa) is shown at three pressure levels, 177, 67 and 23 hPa, separated by roughly one scale height. The lowest level is near the tropopause altitude, the mid-level is in the middle of ozone layer and the highest level is in the upper part of the ozone layer, at an altitude where ozone is strongly affected by photochemistry and

less by dynamics. As expected the lowest ozone values are seen close to the troposphere and the highest in the middle of the ozone layer both in the model and the ozone soundings.

The comparisons again show that the general performance of the FinROSE model is good as the agreement with observations is reasonable. Some differences can be seen in the ozone data between the stations, Payerne a northern hemispheric mid-latitude station (Fig. 3) and Syowa a high latitude southern hemispheric station (Fig. 4). As expected, there is on average more ozone in the Payerne data. Relative month-to-month variations are well simulated both above Europe and Antarctica. The concentration of ozone is generally quite well simulated, however at 23 hPa the model exhibits a negative bias of around 2 mPa at Payerne. At mid-latitudes the model typically shows a negative bias above ca. 50 hPa, which results in a total ozone deficiency (Figs. 1 and 2). The ozone at lower altitudes above Europe is well simulated, both the level and the amplitude of the seasonal variations is good. For Syowa there is no clear bias on any level but the amplitude of the seasonal variations is smaller in the FinROSE results than in the soundings, which is probably partly due to the relatively sparse resolution of the model. The inflow of ozone to the high latitudes during the southern hemispheric winter is clearly too weak in the model simulation. The severity of the Antarctic ozone depletion increases towards the 1990s, which can be seen from both soundings and model data.

Ozone depletion processes

Chlorine activation due to heterogeneous reactions caused by PSCs is the main reason for polar ozone loss. The heterogeneous processing releases chlorine from the so called storage compounds like HCl or $ClONO_2$. The catalytic ozone depleting cycles are initiated when the polar vortex area becomes sunlit. The PSCs can also cause denitrification (or dehydration) by gravitational sedimentation. This process decreases the probability of reaction between ClO and NO_2, which intensifies and prolongs ozone depletion season by increasing the efficiency of the catalytic ozone depleting cycles. The situation in the wintertime and springtime northern high-latitude stratosphere is far less favourable for PSC formation than in the south as the temperatures do not exhibit sufficiently low values regularly. The study of more subtle Arctic ozone loss is a good sensitivity test for a model like FinROSE.

The models ability to describe polar ozone loss was estimated by looking at the evolution of total ozone as well as chlorine activation, PSC occurrences and ozone loss percentages at the 450 K potential temperature level from mid January until mid February during the 1999/2000 winter (Fig. 5). The vortices are indicated by the 36 PVU isoline. According to northern hemisphere standards this particular winter exhibited a cold stable polar vortex and therefore also numerous studies about this winter exist (*see* e.g. references listed in WMO 2003). The anomalously cold northern hemispheric polar vortex resulted in high chlorine activation levels and subsequently relatively severe ozone loss. The result of the cold vortex is quite self-evident: Over the areas where PSC occurrence is high within the vortex area the respective chlorine activation exceeds 80% (Fig. 5). However, the polar night, and the non-existence of solar energy prevent ozone depletion processes during mid-January (lower leftmost panel in Fig. 5). During early February some solar energy becomes available along the edges of the vortex (middle column lowest panel in Fig. 5), and thus ozone depletions up to 20% are seen at the 450 K level. Later on, during mid-February (rightmost column, lowest panel in Fig. 5), the availability of the solar energy increases and the ozone depletion percentages grow up to 30%. Also due to the mixing processes the whole vortex area exhibits elevated ozone depletion percentages.

As for the North, data for ozone depletion, chlorine activation and PSC occurrences in the southern hemispheric wintertime and springtime vortex were studied (Fig. 6). Note, however, the different time-interval for the southern vortex. Values are now given for early August, early September and early October at 450 K potential temperature surface. Several typical differences can bee seen between the hemispheres. The hemispheric differences in land–sea contrasts, orographic differences and resulting differences

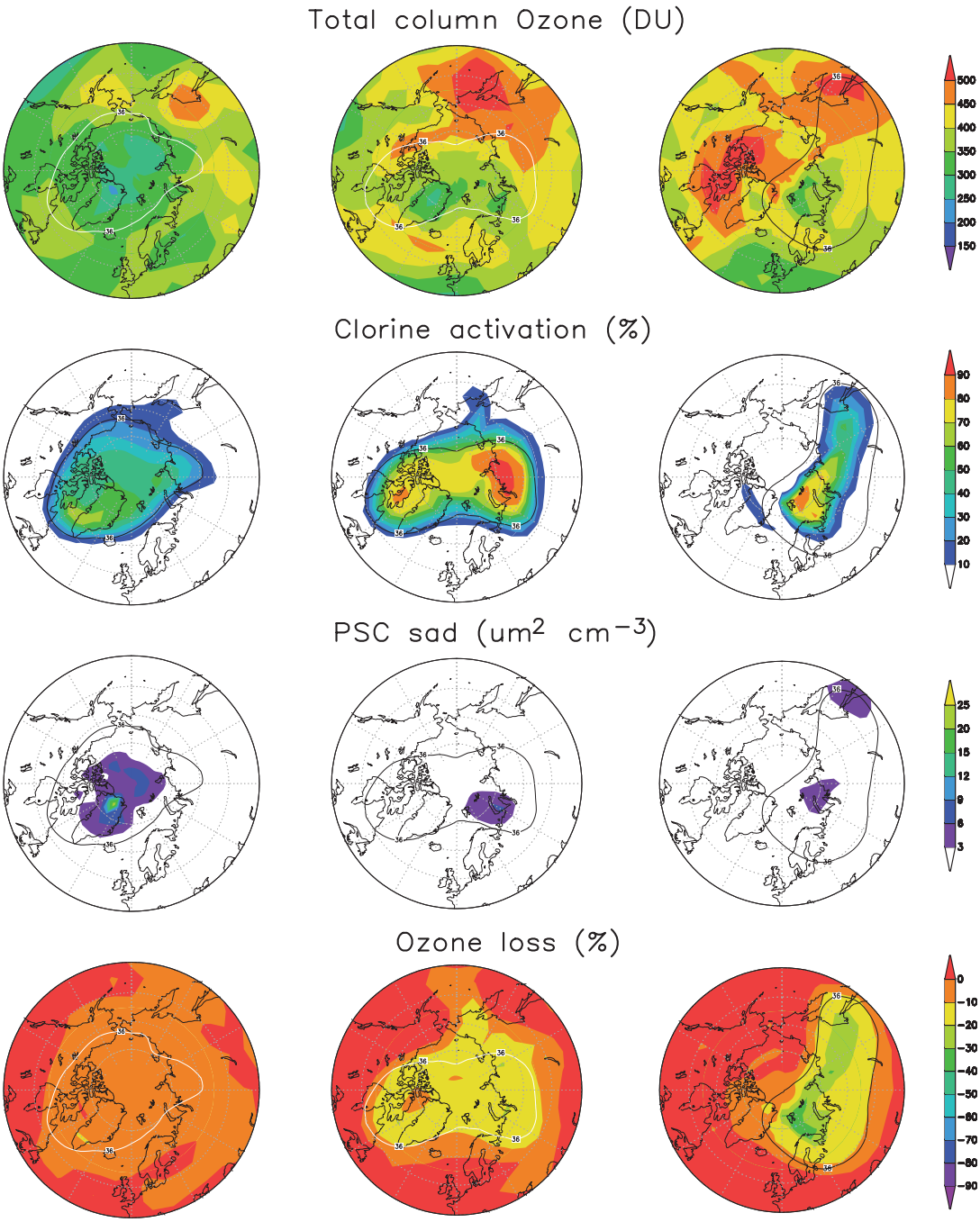

Fig. 5. The evolution of ozone and key parameters for ozone loss during the 1999/2000 northern hemispheric winter and spring shown as daily averages at the 450 K potential temperature level. Total column ozone (DU) in the uppermost row, chlorine activation (%) in the second row, PSC surface area density ($\mu m^2\ cm^{-3}$) in the third row and ozone loss (%) in the bottom row. First column 17 January, second column 2 February and third column 18 February in 2000. The 36 PVU isoline indicates the vortex edge at 450 K.

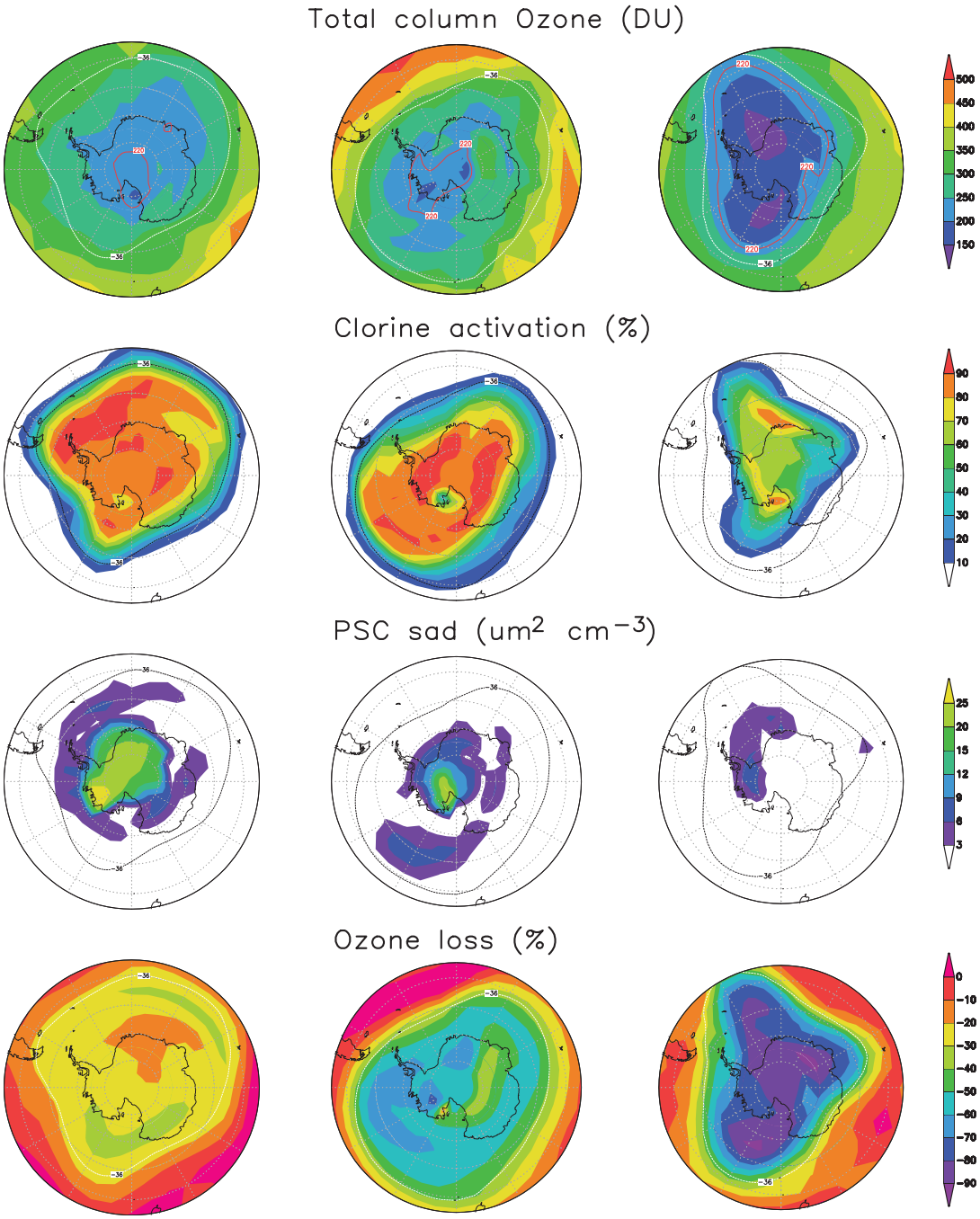

Fig. 6. The evolution of ozone and key parameters for ozone loss during the 2000 southern hemispheric winter and spring, shown as daily averages at the 450 K potential temperature level. Total column ozone (DU) in the uppermost row, chlorine activation (%) in the second row, PSC surface area density (μm^2 cm^{-3}) in the third row and ozone loss (%) in the bottom row. First column 2 August, second column 1 September and third column 1 October in 2000. The –36 PVU isoline indicates the vortex edge at 450 K and the 220 DU isoline indicates the 'ozone hole'.

in atmospheric flow patterns cause the northern vortex to become less symmetrical, smaller in geographical extent, generally warmer and less stable than the southern polar vortex. The northern hemispheric polar vortex forms typically in late November and breaks up by mid-March, while the southern hemispheric polar vortex lasts for about 7 months from May to November. In general, within the southern vortex the high chlorine activation and persistence of the Ant-Arctic vortex results in a severe ozone loss (Fig. 6). The simulated ozone depletion reaches up to 80%–100% at certain altitudes, which gives total column ozone values below 150 DU and ozone mixing ratios of less than 0.5 ppmv at 450 K surface within the Antarctic vortex. The size of the Antarctic 'ozone hole' is indicated with the 220 DU isoline in (Fig. 6). In general, the ozone loss in September in the southern hemisphere and in March in the northern hemisphere is somewhat underestimated in the model simulation (no comparison with observations shown here). Over the southern hemisphere the Brewer-Dobson circulation is weaker than over the northern hemisphere and therefore the overall level of the column ozone is also lower over the southern vortex (topmost rows in Figs. 5 and 6).

The southern wintertime and springtime vortex is typically very stable and persistent and therefore ideal for the formation of PSCs. In fact, while the temperatures within the northern hemispheric polar vortex rarely descend low enough to form water/ice PSCs, these low temperatures occur regularly within the Antarctic vortex. These differences are quite self-evident in the PSC surface area densities (Figs. 5 and 6): Elevated PSC surface area densities are found over the whole vortex domain in the southern case. The consequent chlorine activations and severity of ozone depletion in the south are clearly more profound than in the north. The high PSC surface area densities in the southern hemispheric vortex are actually due to type II PSCs (i.e. water/ice PSCs). Despite the fact that the northern hemispheric 1999/2000 stratospheric winter was cold and the vortex was fairly stable (Fig. 5), the chlorine activation was less profound than in the southern vortex (Fig. 6). As expected, within the southern polar vortex practically complete chlorine activation is exhibited (Fig. 6). Later during the spring when the vortices become warmer the PSC occurrence decreases and therefore also the chlorine activation decreases (last columns in rows 2 and 3, Figs. 5 and 6). The existence of ice-form PSCs in the southern case also means that the process of denitrification becomes possible and effective. This can be seen as the simulated ozone depletion grows even more severe during the spring after the PSC peak period in southern hemispheric winter (Fig. 6). No self-evident signs of such deepening or prolongation of the ozone depletion could be seen in the northern vortex (Fig. 5).

Conclusions

For this study the chemical transport model FinROSE was improved and developed in several ways from its original version (Rose and Brasseur 1989). These improvements included the replacement for the advection scheme, the replacement for the photodissociation calculation scheme, the updates for the chemical kinetics, the improvements for the heterogeneous processing and some updates/improvements for the chemical mechanism of the model.

As a general conclusion it is fair to say that the FinROSE model reproduces the observed global patterns, seasonal variations and year-to-year evolutions of stratospheric ozone well. Also the main stratospheric processes are captured very well in the FinROSE simulations: ozone depletions with PSC formation, chlorine activation and prolongation of the ozone depletion due to denitrification. The differences between the model results and the measurements seem to be connected with limitations and imperfections in model tracer transport (or in the reproduction of the Brewer-Dobson circulation) and with general model design. While some discrepancies between the measurements and model results exist, the results given in "Results and discussion" show that the FinROSE model is capable of simulating realistic behaviour of stratospheric ozone from seasonal scales to decadal scales.

Several applications on the use of FinROSE (or the CTM approach in general) may be easily listed. These applications include the use of the CTM approach for the derivation of the upper

vertical boundary conditions for the GCMs as well as for the CCMs. This idea has been applied in case of the FinROSE model in an EU/FP5 funded project, RETRO (EVK2-CT-2002-00170). CTMs may also be used as a feasible platform for testing new parameterizations and implementations (e.g. PSC schemes and aerosol modules), or they can be used as box model solvers in trajectory type applications. The usage of CTMs as a part of an operational satellite data production system has already been tested. Chemical data assimilation of satellite measurements into operational atmospheric air quality models and applications is also in the range of CTM usage. One possibility could be a CCM/GCM parallel CTM code to be used as an interpreter or intelligent analyzer of the CCM/GCM results.

Acknowledgements: The funding received through the projects EU/EuroSPICE (EVK2-CT-1999-00014), EU/CANDIDOZ (EVK2-CT-2001-00133), EU/RETRO (EVK2-CT-2002-00170), EU/QUOBI (EVK2-CT-2001-00129), SA/FAUVOR II and SA/FARPOCC is gratefully acknowledged. The authors whish to thank Prof. G. Brasseur for providing the original model code and valuable guidance. The ozone soundings data was retrieved from the NILU RETRO data base. The authors are grateful to the data originators (TOMS team and ECMWF).

References

Atkinson R., Baulch D.L., Cox R.A., Hampson R.F., Kerr J.A., Rossi M.J. & Troe J. 2000. Evaluated kinetic and photochemical data for atmospheric chemistry: Supplement VIII, Halogen species — IUPAC subcommittee on gas kinetic data evaluation for atmospheric chemistry. *Journal of Physical and Chemical Reference Data* 29: 167–266.

Austin J., Butchart N. & Shine K.P. 1992. Possibility of an Arctic ozone hole in a doubled-CO_2 climate. *Nature* 360: 221–225.

Bekki S. & Pyle J. 1992. Two-dimensional assessment of the impact of aircraft sulphur emissions on the stratospheric sulphate aerosol layer. *J. Geophys. Res.* 9: 15839–15847.

Brasseur G.P., Granier C. & Walters S. 1990. Future changes in stratospheric ozone and the role of heterogeneous chemistry. *Nature* 348: 626–628.

Crutzen P. & Arnold F. 1986. Nitric acid cloud formation in the cold Arctic stratosphere, a major cause for the springtime "ozone hole". *Nature* 324: 651–655.

Carslaw K.S., Luo B. & Peter T. 1995. An analytic expression for the composition of aqueous HNO_3–H_2SO_4 stratospheric aerosols including gas phase removal of HNO_3. *Geophys. Res. Lett.* 22: 1877–1880.

Chipperfield M.P. 1999. Multiannual simulations with a three dimensional chemical transport model. *J. Geophys. Res.* 104: 1781–1805.

Chipperfield M.P. 2003. A three-dimensional model study of long-term mid-high latitude lower stratosphere ozone changes. *Atmos. Chem. Phys.* 3: 1–13.

Chipperfield M.P. 2006. New version of the TOMCAT/SLIMCAT off-line chemical transport model: Intercomparison of stratospheric tracer experiments. *Q. J. R. Meteorol. Soc.* 132: 1179–1203.

Damski J. 2005. *A chemistry-transport model simulation of the stratospheric ozone for 1980 to 2019*. Ph.D. thesis, University of Helsinki.

DeMore W.B., Sander S.P., Golden D.M., Hampson R.F., Kurylo M.J., Howard C.J., Ravishankara A.R., Kolb C.E. & Molina M.J. 1997. *Chemical kinetics and photochemical data for use in stratospheric modeling, evaluation number 12*. JPL Publication 97-4.

Dethof A. & Hólm E. 2004. Ozone assimilation in the ERA-40 reanalysis project. *Q. J. R. Meteorol. Soc.* 130: 2851–2872.

Dye J.E., Baumgardner D., Gandrud B.W., Kawa S.R., Kelly K.K., Loewenstein M., Ferry G.V., Chan K.R. & Gary B.L. 1992. Particle size distributions in arctic polar stratospheric clouds, growth and freezing of sulfuric acid droplets, and implications for cloud formation. *J. Geophys. Res.* 97: 8015–8034.

Egorova T.A., Rozanov E., Schlesinger M., Andronova,N., Malyshev S., Karol I. & Zubov V. 2001. Assessment of the effect of the Montreal Protocol on atmospheric ozone. *Geophys. Res. Lett.* 28: 2389–2392.

Fahey D.W., Solomon S., Kawa S.R., Loewenstein M., Podolske J.R., Strahan S.E. & Chan K.R. 1990. A diagnostic for denitrification in the winter polar stratosphere. *Nature* 345: 698–702.

Fahey D.W., Gao R.S., Carslaw K.S., Kettleborough J., Popp P.J., Northway M.J., Holecek J.C., Ciciora S.C., McLaughlin R.J., Thompson T.L., Winkler R.H., Baumgardner D.G., Gandrud B., Wennberg P.O., Dhaniyala S., McKinney K., Peter Th., Salawitch R.J., Bui T.P., Elkins J.W., Webster C.R., Atlas E.L., Jost H., Wilson J.C., Herman R.L., Kleinböhl A. & von König M. 2001. The detection of large nitric-acid particles in the winter Arctic stratosphere. *Science* 291: 1026–1031.

Fortuin J.P. & Kelder F.H. 1998. An ozone climatology based on ozonesonde and satellite measurements. *J. Geophys. Res.* 103: 31709–31734.

Hanson D. & Mauersberger K. 1988. Laboratory studies of the nitric acid trihydrate: Implications for the south polar stratosphere. *Geophys. Res. Lett.* 15: 855–858.

Jackman C.H., Fleming E.L., Chandra S., Considine D.B. & Rosenfield J.E. 1996. Past, present, and future modeled ozone trends with comparisons to observed trends. *J. Geophys. Res.* 101: 28753–28768.

Krämer M., Müller R., Bovensmann H., Burrows J., Brinkmann J., Röth E.-P., Grooß J.-U., Müller R., Woyke T., Ruhnke R., Günther G., Hendricks J., Lippert E., Carslaw K.S., Peter T., Zieger A., Brühl C., Steil B.,

Lehmann R. & McKenna D.S. 2003. Intercomparison of stratospheric chemistry models under polar vortex conditions. *J. Atmos. Chem.* 45: 51–77.

Kylling A. 1992. *Radiation transport in cloudy and aerosol loaded atmosphere*. Ph.D. thesis, University of Alaska.

Kylling A., Albold A. & Seckmeyer G. 1997. Transmittance of a cloud is wavelength-dependent in the UV-range: Physical interpretation. *Geophys. Res. Lett.* 24: 397–400.

Lefèvre F., Figarol F., Carslaw K.S. & Peter T. 1998. The 1997 Arctic ozone depletion quantified from three-dimensional model simulations. *Geophys. Res. Lett.* 25: 2425–2428.

Lin S.-J. & Rood R.B. 1996. Multidimensional flux-form semi-lagrangian transport schemes. *Mon. Weather Rev.* 124: 2046–2070.

Lin S.-J., Chao W.C., Sud Y.C. & Walker G.K. 1994. A class of the van Leer-type transport schemes and its applications to the moisture transport in a General Circulation Model. *Mon. Weather Rev.* 122: 1575–1593.

McLinden C.A., McConnell J.C., McElroy C.T. & Griffioen E. 1999. Observations of stratospheric aerosol using CPFM polarized limb radiances. *JAS* 56: 233–240.

Marti J. & Mauersberger K. 1993. A survey and new measurements of ice vapor pressure at temperatures between 170 and 250 K. *Geophys. Res. Lett.* 20: 363–366.

Mayer B., Kylling A., Madronich S. & Seckmeyer G. 1998. Enhanced absorption of UV radiation due to multiple scattering in clouds: Experimental evidence and theoretical explanation. *J. Geophys. Res.* 103: 31241–31254.

Rose K. & Brasseur G. 1989. A three-dimensional model of chemically active trace species in the middle atmosphere during disturbed winter conditions. *J. Geophys. Res.* 94: 16387–16403.

Rosenfield J.E., Considine D.B., Meade P.E., Bacmeister J.T., Jackman C.H. & Schoeberl M.R. 1997. Stratospheric effects of Mount Pinatubo aerosol studied with a coupled two-dimensional model. *J. Geophys. Res.* 102: 3649–3670.

Rummukainen M., Isaksen I.S.A., Rognerud B. & Stordal F. 1999. A global model tool for three-dimensional multiyear stratospheric chemistry simulations: Model description and first results. *J. Geophys. Res.* 104: 26437–26456.

Sander S.P., Finlayson-Pitts B.J., Friedl R.R., Golden D.M., Huie R.E., Kolb C.E., Kurylo M.J., Molina M.J., Moortgat G.K., Orkin V.L. & Ravishankara A.R. 2002. Chemical kinetics and photochemical data for use in atmospheric studies, evaluation number 14. *JPL Publication* 02-25.

Shindell D.T., Rind D. & Lonergan P. 1998. Increased polar stratospheric ozone losses and delayed eventual recovery owing to increasing greenhouse-gas concentrations. *Nature* 392: 589–592.

Shine K.P., Bourqui M.S., Forster P.M.D., Hare S.H.E., Langematz U., Braesicke P., Grewe V., Schnadt C., Smith C.A., Haigh J.D., Austin J., Butchart N., Shindell D., Randel W.J., Nagashima T., Portmann R.W., Solomon S., Seidel D., Lanzante J., Klein S., Ramaswamy V. & Schwarzkopf M.D. 2003. A comparison of model-predicted trends in stratospheric temperatures. *Q. J. R. Meteorol. Soc.* 129: 1565–1588.

Simmons A.J. & Gibson J.K. 2000. The ERA-40 Project Plan. *ERA-40 Project Report Series* no. 1.

Smith A.K. 1995. Numerical simulation of global variations of temperature, ozone, and trace species in the stratosphere. *J. Geophys. Res.* 100: 1253–1270.

Solomon S. 1999. Stratospheric ozone depletion: A review of concepts and history. *Rev. Geophys.* 37: 275–316.

Solomon S., Garcia R.R., Rowland F.S. & Wuebbles D.J. 1986. On the depletion of Antarctic ozone. *Nature* 321: 755–758.

UNEP 2000. *The Montreal Protocol on substances that deplete the ozone layer as adjusted and/or amended in London 1990, Copenhagen 1992, Vienna 1995, Montreal 1997, Beijing 1999*, Ozone Secretariat, United Nations Environment Programme.

Van Noije T.P.C, Eskes H.J., Van Weele M. & Van Velthoven P.F.J. 2004. Implications of the enhanced Brewer-Dobson circulation in European Centre for medium-range weather forecasts reanalysis ERA-40 for the stratosphere-troposphere exchange of ozone in global chemistry transport models. *J. Geophys. Res.* 109, D19308, doi: 10.1029/2004JD004586.

WMO 2003. *Scientific assessment of ozone depletion: 2002, Global Ozone Research and Monitoring Project*. Report No. 47, Geneva.

Zalesak S.T. 1979. Fully multidimensional flux-corrected transport algorithms for fluid. *J. Comput. Phys.* 31: 335–362.